Steady and unsteady loading and radiated far-field sound of three NACA series airfoils in a uniform flow

J.A. Branch[1], B. Zang[2], and M. Azarpeyvand[3]
Faculty of Engineering, University of Bristol, BS8 1TR, United Kingdom

Edward Jinks[4]
Dowty Propellers, United Kingdom

Michelle Fernandino Westin[5]
Embraer S.A, Brazil

This paper investigates the hydrodynamic near-field and predicted radiated acoustic far-field of three NACA-series airfoils, namely the NACA 16-616, NACA 16-506, and NACA 0024 profiles, over a range of angles of attack, encompassing the pre-stall, stall, and post-stall flow regimes. In both the static pressure and the pressure fluctuation results, it is shown that each flow regime for each airfoil is easily distinguished, that each regime has different spectral behavior and boundary layer characteristics, and it is further shown that the behavior is different for each airfoil. In particular, it is shown that airfoil shape has a significant impact on both the angle of attack at which stall occurs and on the nature of the stalling mechanism. In the predicted radiated acoustic field, it is found that the variation of sound pressure level with frequency and with angle of attack is different for each airfoil, with airfoil thickness shown to have a significant impact on the abrupt effect of stall on the predicted radiated far-field sound. This is of significance due to the widespread use of aeroacoustic models, such as that proposed by Brooks, Pope, and Marcolini, derived empirically from only one airfoil.

I. Nomenclature

c	[m]	Airfoil chord length
C_L	[-]	Lift coefficient
C_P	[-]	Pressure coefficient
$C_{p,rms}$	[-]	Root-mean-square pressure coefficient
d	[m]	Airfoil span
f	[Hz]	Frequency
h	[mm]	Nozzle exit height
$l(f)$	[m]	Spanwise coherence length
L	[N]	Numerically integrated lift force
M	[-]	Mach number
p	[Pa]	Static pressure
PSD	-	Power spectral density
RMS	-	Root-mean-square
Re_c	[-]	Chord-referenced Reynolds number
St	[-]	Strouhal number
t	[s]	Time
u	[ms^{-1}]	Velocity
U_∞	[ms^{-1}]	Freestream velocity

[1] PhD student, Department of Aerospace Engineering, University of Bristol. john.branch@bristol.ac.uk.
[2] Lecturer, Department of Aerospace Engineering, University of Bristol. nick.zang@bristol.ac.uk.
[3] Professor, Department of Aerospace Engineering, University of Bristol. m.azarpeyvand@bristol.ac.uk.
[4] Performance Team Lead, Dowty Propellers. edward.jinks@ge.com
[5] Product Development Engineer, Embraer S.A. michelle.westin@embraer.com.br.

w	[mm]	Nozzle exit width
x	-	Chordwise direction
y	-	Spanwise direction
z	-	Direction normal to chord line
α	[°]	Geometric angle of attack
γ^2	[-]	Coherence
δ	[m]	Boundary layer thickness at 99% of freestream velocity
ξ	[m]	Microphone separation distance
ρ	[kgm^{-3}]	Density of air
τ_c	[s]	Temporal correlation scale
ϕ_{pp}	[Pa^2]	Surface pressure fluctuation power spectral density

II. Introduction

The source of airfoil self-noise is classically regarded to be the scattering of boundary layer turbulent disturbances into acoustic waves as they convect past the geometrical discontinuity of the airfoil trailing-edge [1, 2]. Trailing-edge noise, and various methods to reduce it, have been extensively investigated since the advent of aeroacoustic research [3, 4, 5, 1, 6, 7]. This is largely due to the dominance of this noise mechanism in most applications when operating in typical conditions [8, 9]. Many models of airfoil self-noise relate the radiated far-field sound to the near-field hydrodynamics. In the seminal work by Amiet [3], an analytical model to predict airfoil trailing-edge noise was developed by formulating the scattered far-field noise using the airfoil response function and inputs from the incident unsteady pressure spectra and spanwise correlation length of the flow. The model established the significance of the hydrodynamic near-field in the understanding and modelling of the radiated far-field sound.

Airfoils are not typically operated within the stall regime and, consequently, separation and stall noise has received comparatively less attention than the more frequently encountered laminar- and turbulent-boundary layer induced self-noise mechanisms [8]. However, separation and stall noise can still occur in industrially relevant applications since maximum aerodynamic performance is often at high angles of attack, near to stall. For instance, when the pressure rise across an axial compressor fan increases to such an extent that the flow reverses and separates, or when a wind turbine blade encounters flow heavily disturbed by an upstream turbine [10, 11, 12]. Additionally, when separation and stall noise does occur it can be expected to produce higher overall sound levels, particularly at lower frequencies [13, 12, 14], thereby underlining the importance of developing an understanding of the underlying physics of separation and the near-field hydrodynamics to allow future modelling of the radiated far-field stall noise.

Much research into separation-stall noise categorizes the noise into two regimes: (a) *light stall*, where, although there is separation, there is still an attached mean flow over part of the airfoil and noise is radiated primarily from the trailing-edge; and (b) *deep stall*, where the airfoil is fully stalled (aerodynamically) with mean recirculation over the airfoil, and the noise is also radiated from the whole chord in a manner similar to a bluff body [8, 15, 12]. As is the case for trailing-edge noise, the flow features in the boundary layer of the airfoil, and their surface pressure imprint on the airfoil, are the origin of the radiated far-field noise. Consequently, understanding of the physics of the far-field noise, crucial for the development of any model of this noise, is contingent on understanding of the hydrodynamic near-field [1, 6, 16, 17, 12]. In recent years, high-fidelity near-field hydrodynamic data has been collected for a range of airfoils, such as various flat plates, symmetric NACA 0012 and NACA 0021 profiles as well as cambered airfoils such as the NACA 65-1210, NACA 65-(12)10, and NACA 65-410 profiles [12, 8, 9, 18, 19]. The spectral near-field hydrodynamic behavior is strongly dependent on airfoil shape, and so for the development of generalized far-field noise models, high-fidelity near-field hydrodynamic data for a range of airfoils is pivotal.

The BPM model [20], though widely used in industry [21, 22], is empirically derived from NACA 0012 data and so cannot be expected to provide an accurate model of the radiated far-field noise of airfoils different in shape to the NACA 0012 profile. Consequently, the collection and dissemination of near-field hydrodynamic data for a wide range of airfoils is vital for the development of future models of separation and stall noise. This is the context of the present study, where highly instrumented NACA 16-616, NACA 16-506, and NACA 0024 airfoils have been experimentally investigated in a range of operating conditions as described subsequently.

This paper will investigate the hydrodynamic near-field and predicted radiated acoustic far-field of the NACA 16-616, NACA 16-506, and NACA 0024 airfoil profiles. In what follows; Section III presents an overview of the experimental setup of the present study; Section IV subsequently details the static pressure results for each airfoil, providing insights into each's stalling behavior; Section V then presents the surface pressure fluctuation results, providing a higher fidelity insight into the nature of the flow around the airfoils; Section VI provides a more direct insight into the velocity fluctuations that are the origin of the near-field surface pressure fluctuations via boundary

layer velocity measurements; Section VII presents predicted far-field sound results; and finally, Section VIII concludes the paper.

III. Experimental Setup

The experiment was conducted in the aeroacoustic open-jet wind tunnel facility at the University of Bristol. The wind tunnel is located within a chamber that is anechoic for frequencies above 160Hz. The design and performance of the wind tunnel facility are summarized in Mayer et al [23]. For this study, a rectangular nozzle with exit dimensions of height $h = 775\text{mm}$ and width $w = 500\text{mm}$ was employed. Figure 1(a) provides an overview of the test section mounted within the anechoic facility and flush mounted to the nozzle exit, with a beamforming array positioned above it for far-field noise measurement. Figure 1 (b) shows the NACA 16-616 airfoil installed within the test section and the tensioned Kevlar panels that form the top and bottom walls of the test section, the NACA 16-506 and NACA 0024 airfoils were installed in an identical manner. These Kevlar walls are effectively acoustically transparent, allowing acoustic waves to pass through whilst greatly reducing flow deflection in a similar manner to a solid-walled closed test section [24]. This minimization of flow deflection allows for far greater effective angles of attack to be achieved than in the classical open-jet configuration, crucially important for the study of stall noise. It has been shown that the geometric airfoil angle of attack can be translated to free-air equivalent effective angles of attack [30, 31], though for the present study it was found that these corrections were of the order of $\sim 0.5\%$ and so geometric angles of attack are presented in this paper.

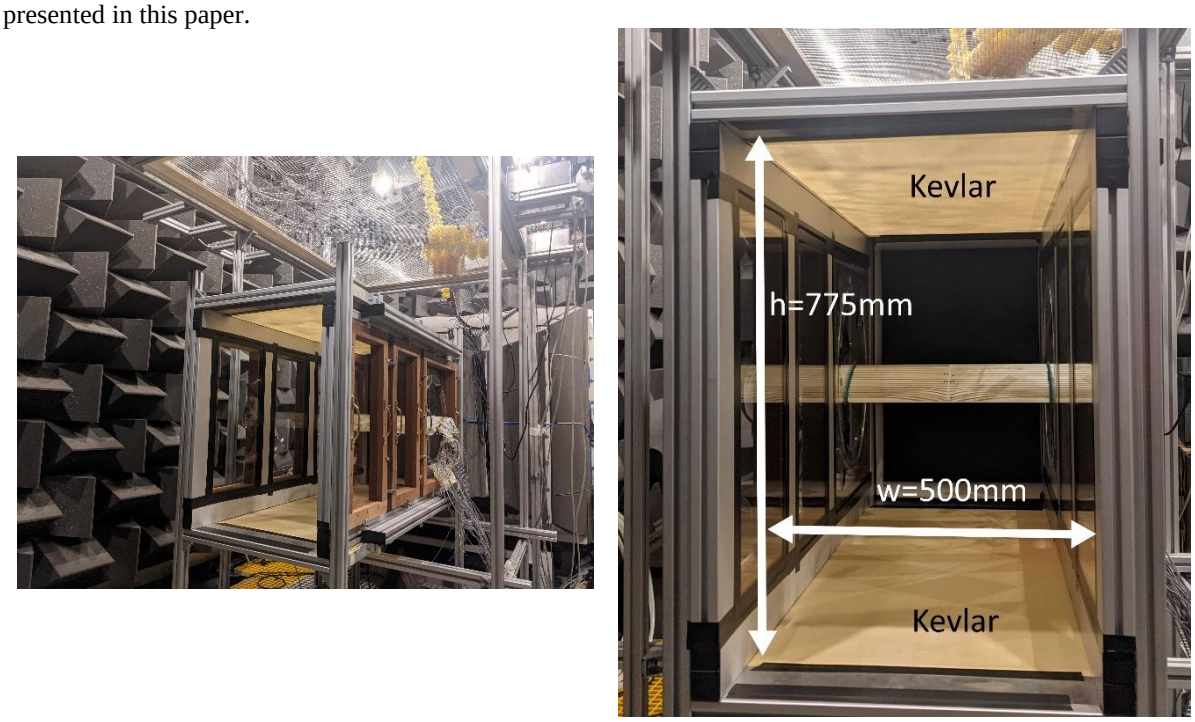

(a) (b)

Figure 1: (a) test section mounted to nozzle exit with beamforming array above, and (b) the test section as viewed from a downstream position with the NACA 16-616 airfoil installed.

For each airfoil, static pressure and unsteady surface pressure fluctuations are measured remotely using brass tubes, resin-sealed into the airfoil surface, with 0.4mm pinholes aligned with the center-section of the airfoil span across the chord. Figure 2 shows the chordwise and spanwise distributions of the unsteady surface pressure fluctuation measurement locations for each airfoil, showing the high concentration on the airfoil suction surface and the spanwise distribution at the trailing-edge.

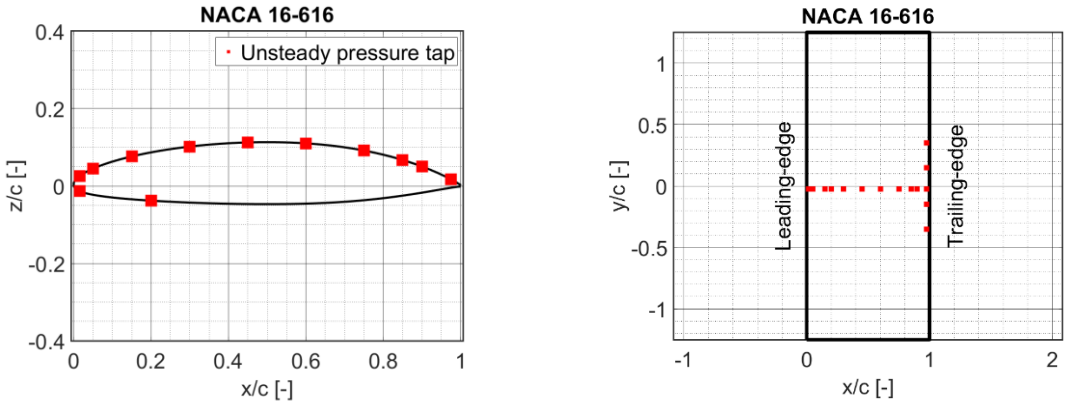

(a)

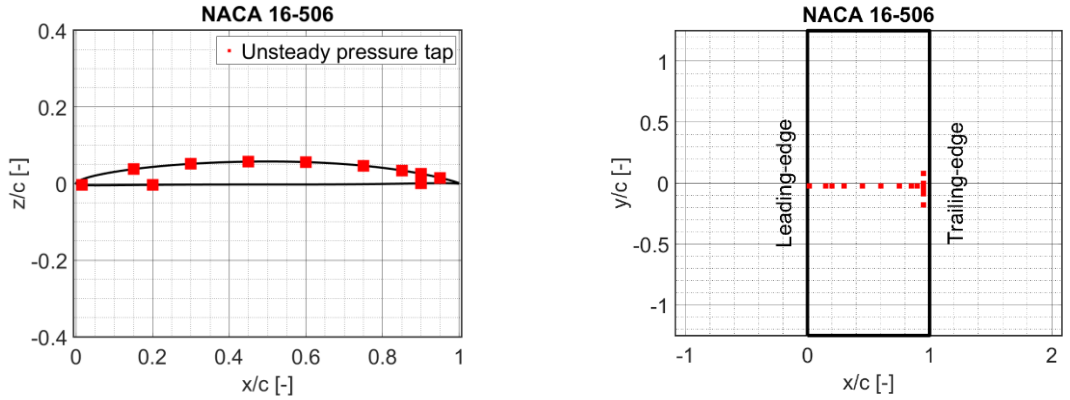

(b)

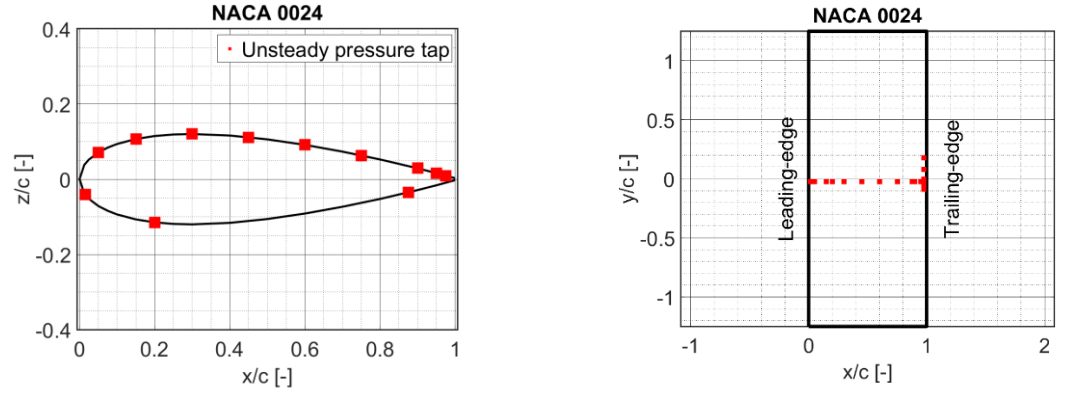

(c)

Figure 2: (a) NACA 16-616 airfoil profile and planform with unsteady pressure tap locations indicated, (b) NACA 16-506 airfoil profile and planform with unsteady pressure tap locations indicated, and (c) NACA 0024 airfoil profile and planform with unsteady pressure tap locations indicated.

IV. Static Pressure Results

This section provides an overview of the variation of the mean static pressure distribution over the NACA 16-616, NACA 16-506, and NACA 0024 airfoil surfaces with the geometric angle of attack. Figures Figure 3,Figure 4, and Figure 5 show the static pressure coefficient distributions at four different angles of attack for each of the three airfoils. For each airfoil the three distinct flow regimes are readily identifiable in the static pressure coefficient: the pre-stall regime is characterized by suction peak growth and a whole-chord reduction in suction surface static pressure as the angle of attack is increased, the stall regime is then characterized by a transition from the pre-stall regime to the post-stall regime, itself characterized by a flat static pressure distribution across the chord indicating separated flow. Although the flow regimes are easily identifiable for each airfoil, their exact characteristics vary with the NACA 16-616 and NACA 0024 airfoils stalling very abruptly whereas the NACA 16-506 airfoil stalls much more gradually. This significant difference in behavior can be expected to result in different radiated far-field sound.

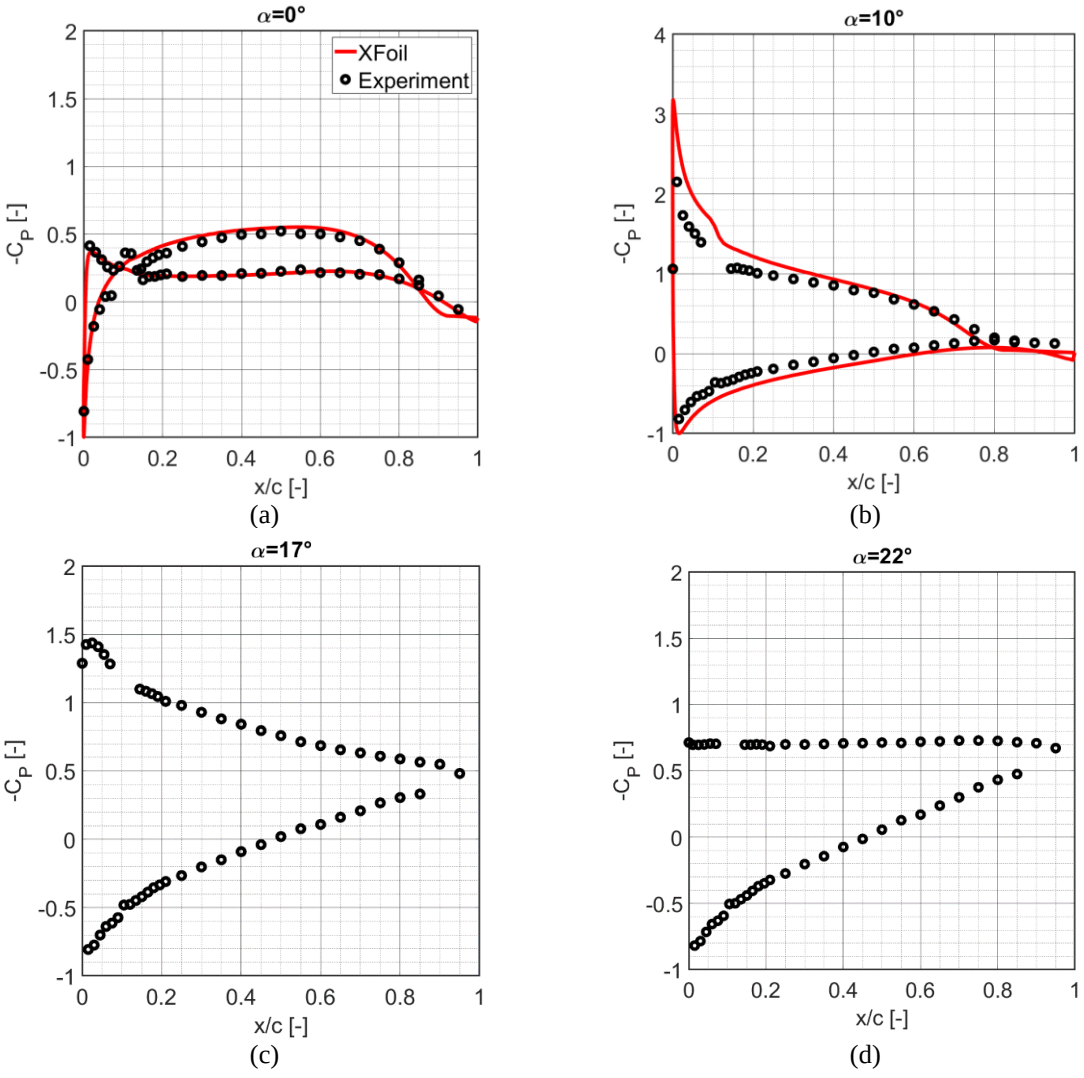

Figure 3: NACA 16-616 static pressure coefficient distribution with XFoil prediction indicated for pre-stall angles at: (a) $\alpha = 0°$, (b) $\alpha = 10°$, (c) $\alpha = 17°$, and (d) $\alpha = 22°$ angles of attack.

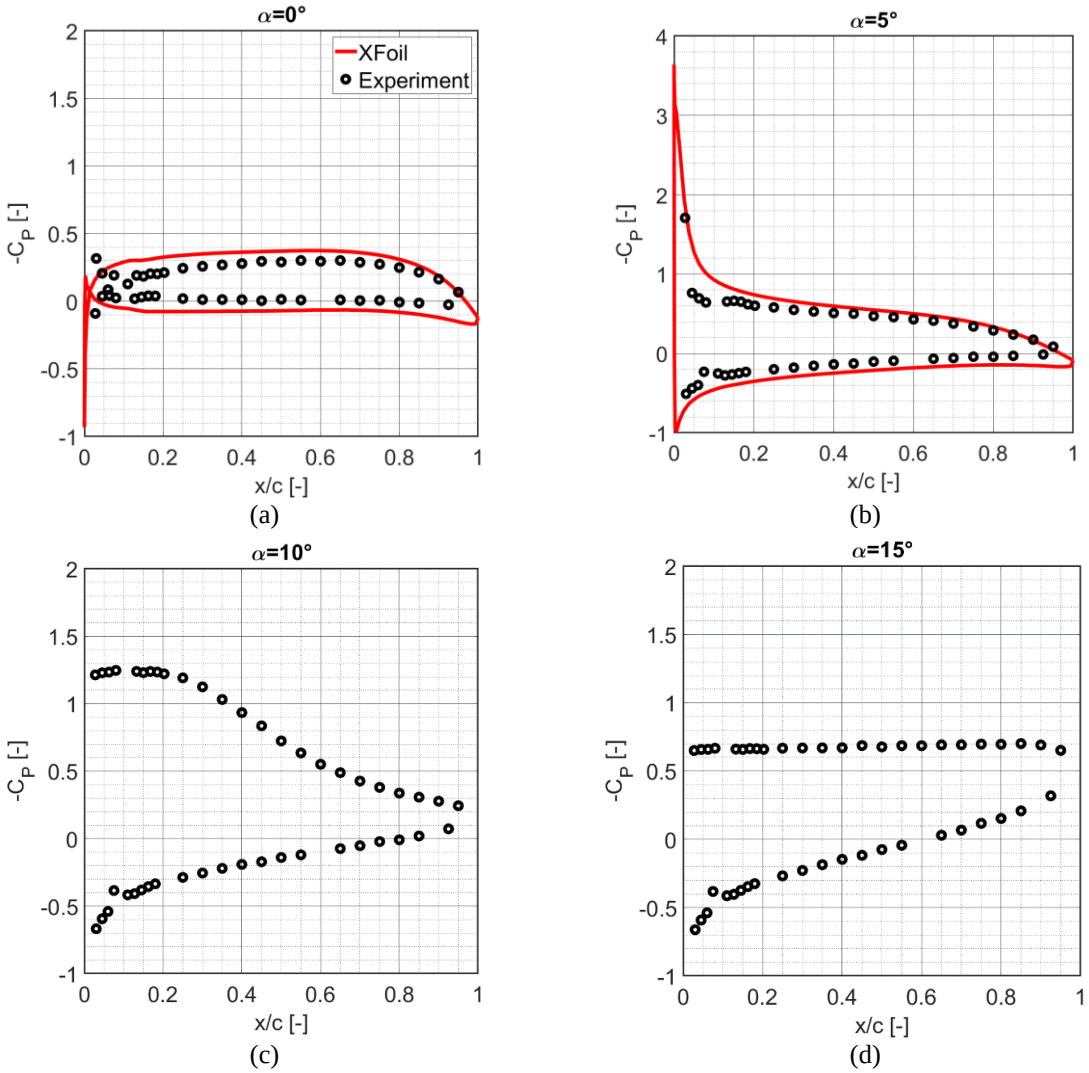

Figure 4: NACA 16-506 static pressure coefficient distribution with XFoil prediction indicated for pre-stall angles at: (a) $\alpha = 0°$, (b) $\alpha = 5°$, (c) $\alpha = 5°$, and (d) $\alpha = 15°$ angles of attack.

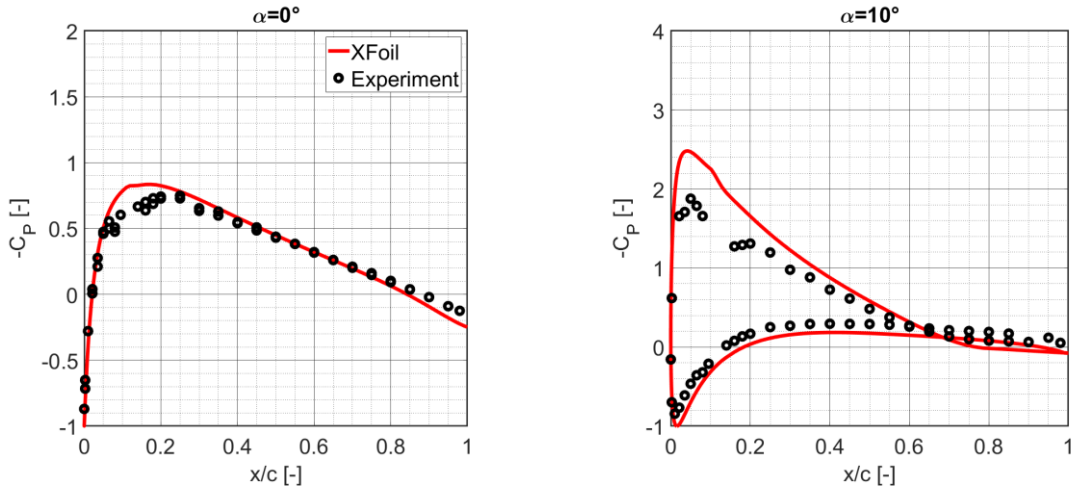

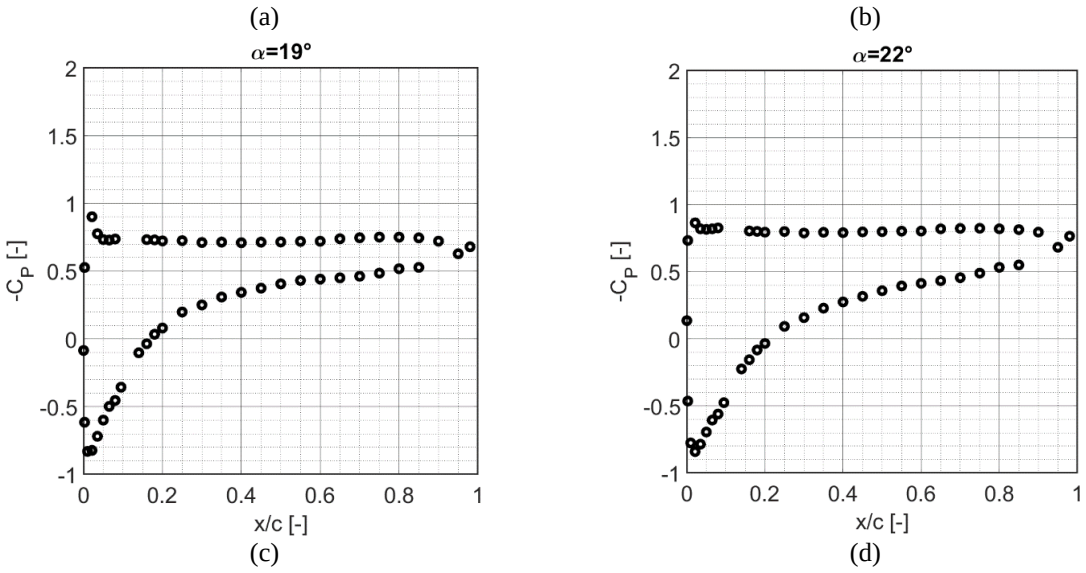

Figure 5: NACA 0024 static pressure coefficient distribution with XFoil prediction indicated for pre-stall angles at: (a) $\alpha = 0°$, (b) $\alpha = 10°$, (c) $\alpha = 17°$, and (d) $\alpha = 22°$ angles of attack.

Figure 6 shows the variation of (i) static-pressure-derived lift coefficient and (ii) its corresponding RMS, for each of the three airfoils. As with the static pressure distributions, these plots show the differing behavior of each airfoil, particularly within the stall regime where the NACA 16-616 and NACA 0024 airfoils can be seen to stall much more abruptly than the thinner NACA 16-506 airfoil.

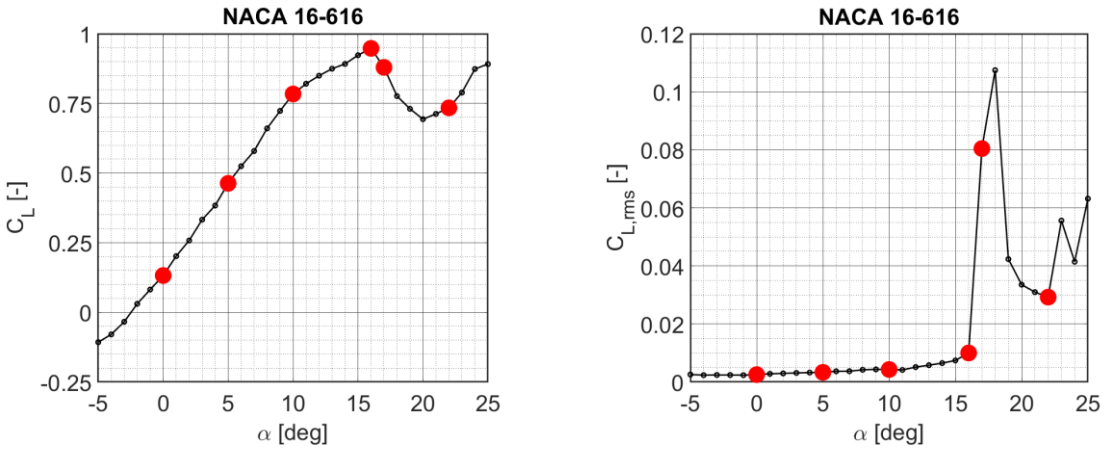

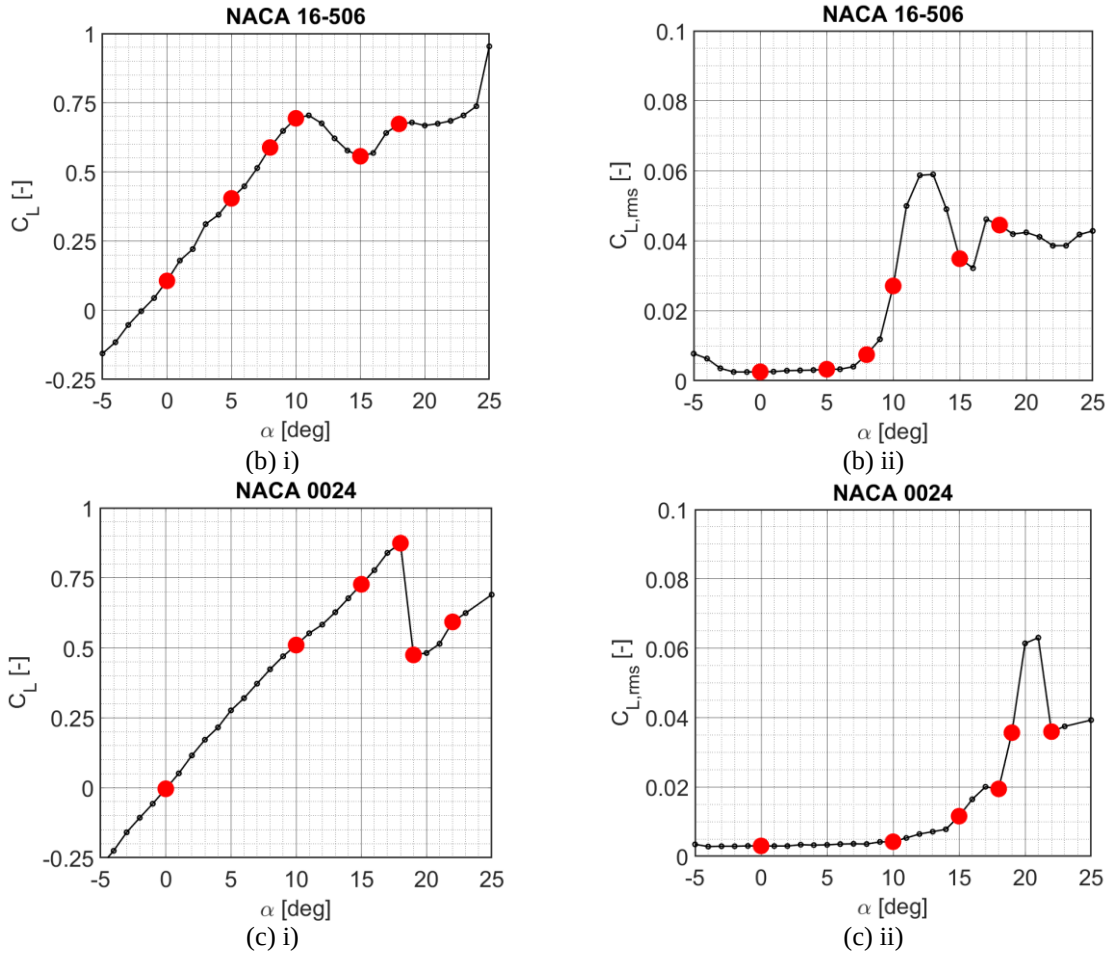

Figure 6: i) Lift coefficient variation with angle of attack and ii) equivalent root-mean-square lift coefficient variation with angle of attack for: (a) NACA 16-616, (b) NACA 16-506, and (c) NACA 0024. Angles of attack to be presented subsequently are indicated in red.

V. Surface pressure fluctuation results

A. Power spectral density of surface pressure fluctuations

This section provides an analysis of the surface pressure fluctuation data recorded for the angles of attack indicated in Figure 6 for each of the three airfoils. Surface pressure fluctuations can be considered the origin of far-field sound, with many hydrodynamic models of airfoil noise relating far-field trailing-edge noise to the power spectral density (PSD) of the surface pressure fluctuations near to the trailing-edge of the airfoil [3] [16] [4] [1]. Additionally, analysis of surface pressure fluctuations across a broad range of frequencies facilitates the development of a deeper understanding of the nature of the boundary layer flow. Consequently, surface pressure fluctuations are a crucial parameter in the field of aeroacoustics and are therefore presented subsequently.

The variation of the NACA 16-616 suction surface pressure fluctuation PSD with angle of attack is shown in Figure 7 for two chordwise positions on the airfoil suction surface: $x/c = 0.75$ and 0.97. As with the previously shown static pressure results, the three distinct flow regimes are readily identifiable in the spectra: pre-stall (for 0° to 15° angles of attack), stall (16° and 17° angles of attack), and post-stall (for angles of attack beyond 17°). The PSD within the pre-stall regime is characterized by broadband spectra with a high-frequency roll-off rate dependent on chordwise position. For the trailing-edge location of $x/c = 0.97$, the spectra decays at a rate of f^{-5} for all angles of attack in the pre-stall regime whereas for further upstream locations this rate of high-frequency decay is only seen at increasingly large angles of attack until, for the $x/c = 0.45$ case, there is no decay at a rate of f^{-5} within the pre-stall regime. The presence of the high frequency roll-off is indicative of the dominance of lower-frequency, large-scale

turbulent structures and so it can be inferred that, towards the trailing-edge, the boundary layers of the NACA 16-616 airfoil are increasingly dominated by large-scale structures, even for very low angles of attack, suggesting a trailing-edge separation mechanism. The change in PSD within the stall regime, for the angles of attack 16° and 17°, is consistent across the airfoil chord with a sharp transition in spectral shape from the pre-stall regime to much higher low frequency levels and a decay rate of $f^{-2.5}$. The spectral behavior is then broadly consistent throughout the post-stall regime except for the development of a peak at a frequency of $f = 50$Hz, corresponding to a frontal-area-referenced Strouhal number of $St = 0.2$, at angles of attack beyond 22°, which has been previously established to be associated with vortex shedding [25].

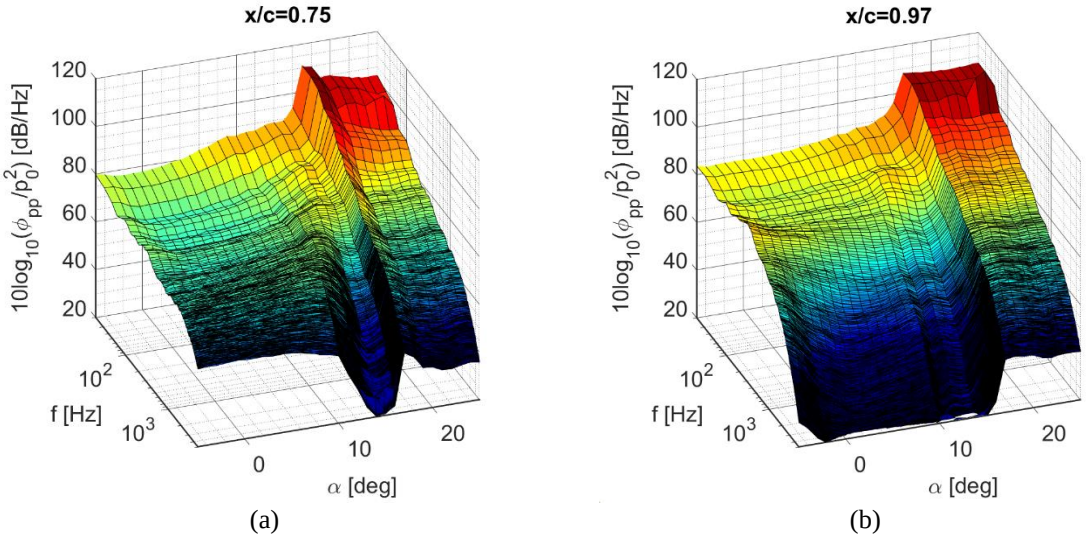

Figure 7: NACA 16-616 surface pressure fluctuations PSD variation with angle of attack at (a) $x/c = 0.75$ and (b) $x/c = 0.97$.

The variation of the NACA 16-506 suction surface pressure fluctuation PSD with angle of attack is shown in Figure 8. As was the case for the NACA 16-616 airfoil, the distinction between each of the three flow regimes is clearly visible for each chordwise position. The pre-stall regime is for angles of attack up to 7°, the stall regime covers angles of attack from 8° to 10°, and all angles of attack beyond 10° are within the post-stall regime.

The pre-stall regime spectra for the NACA 16-506 airfoil are broadband in nature for both chordwise positions and, unlike for the NACA 16-616 airfoil, there is no small-scale separation indicated near to the airfoil's trailing-edge in the spectra. In the pre-stall regime, low frequency levels are consistently $2 - 3$dB lower for the NACA 16-506 airfoil compared to the NACA 16-616 airfoil. The NACA 16-506 stall regime spectral behavior is different to that of the NACA 16-616 airfoil where, instead of an abrupt transition to characteristic stalled flow, there is a much more gradual shift from 8° to 10° angles of attack and levels within the stall regime are markedly higher than those in the pre- and post-stall regimes. This is indicative of high energy surface pressure fluctuations in the stall regime, caused by correspondingly high energy velocity fluctuations in the boundary layer. Post-stall, spectral behavior is very similar to the NACA 16-616 airfoil and again the onset of separated boundary layer vortex shedding is indicated by the peak at $St = 0.2$.

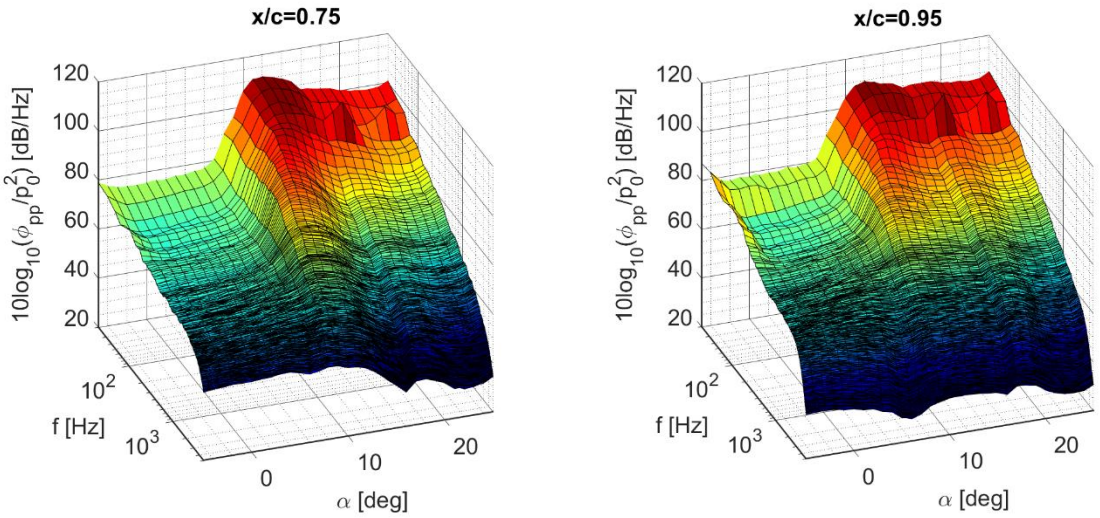

Figure 8: NACA 16-506 surface pressure fluctuations PSD variation with angle of attack at (a) x/c=0.75 and (b) x/c=0.95.

Figure 9 shows the PSD surface contours for the NACA 0024 airfoil suction surface at two chordwise locations: $x/c = 0.75$ and 0.97. The three distinct flow regimes are defined as follows, the pre-stall regime is for angles of attack up to 17°, the stall regime covers angles of attack from 18° to 19°, and all angles of attack beyond 19° are within the post-stall regime.

In the pre-stall regime, NACA 0024 spectral behavior for both chordwise positions is very similar to that of the NACA 16-616 airfoil with a small-scale separation near to the trailing-edge indicated by the reducing high frequency levels as the angle of attack is increased towards stall for near trailing-edge locations. This is as expected due to the thick shape of the NACA 0024 airfoil. The stall regime spectra of the NACA 0024 airfoil are again very similar to the thick NACA 16-616 airfoil with a sharp transition from the pre-stall regime to post-stall, in contrast to the NACA 16-506 airfoil where the transition is more gradual. This sharp transition is indicative of a leading-edge stall mechanism. Post-stall behavior is very similar to the other two airfoils with a higher frequency decay rate of $f^{-2.5}$ and a vortex shedding peak at a Strouhal number of $St = 0.2$.

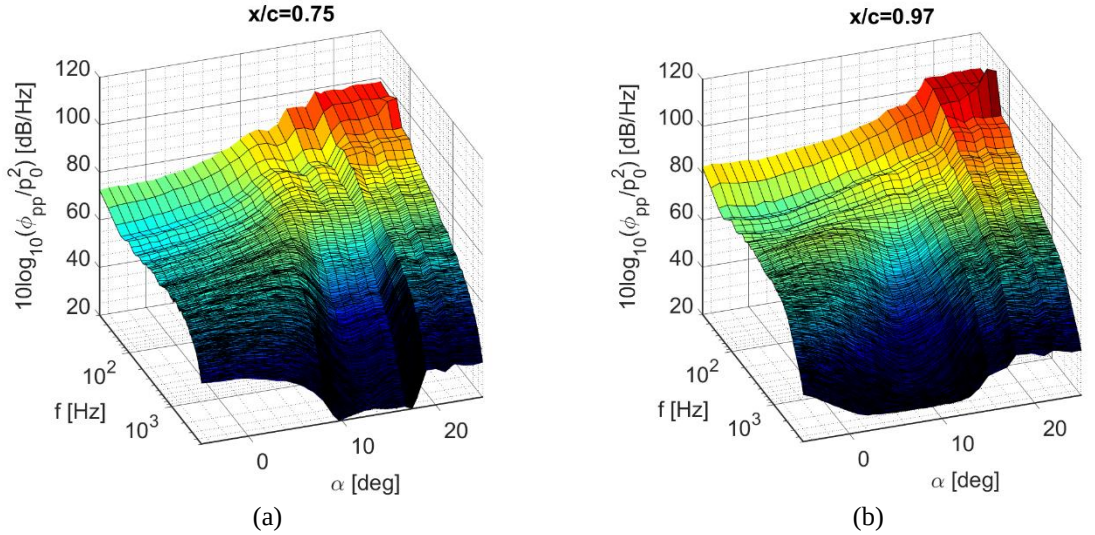

Figure 9: NACA 0024 surface pressure fluctuations PSD variation with angle of attack at (a) x/c=0.75 and (b) x/c=0.97.

B. Spanwise coherence

In addition to the surface pressure fluctuations, another crucial parameter for understanding the structure of the near-field hydrodynamics is the spanwise length scale of the turbulent structures that are convected past the trailing edge [3]. To this end, this section examines the spanwise coherence of the surface pressure fluctuations in the suction surface boundary layer at the trailing-edge of each airfoil and uses this coherence to estimate the spanwise coherence length, a measure of the length scale over which turbulent structures are coherent.

Figure 10(a) shows the spanwise coherence length at the trailing-edge of the NACA 16-616 airfoil for 0°, 5°, and 10° angles of attack, all corresponding to the pre-stall regime, and the positive correlation between coherence length and angle of attack is evident, reflecting the growth in scale of turbulent structures as the angle of attack increases and the boundary layer grows in the pre-stall regime. Figure 10(b) shows the coherence length for the three stall and post-stall regime angles of attack, namely 16°, 17°, and 22°. For the 16° angle of attack case, the spectral shape of the coherence length is very similar to the 10° case except the peak length is more than double the pre-stall case. This reflects that the overall boundary layer behavior at these two angles of attack is similar except for the further development of the secondary trailing-edge separation mechanism for the 16° angle of attack case, as was also evident in the PSD and autocorrelation results previously discussed. Conversely, the 17° and 22° angles of attack cases show a very different spectral shape with a very clear peak coherence length, reflecting that these angles of attack are after the dominant leading-edge stall mechanism has occurred, with the peak coherence length for both angles of attack occurring at the previously noted vortex shedding frequency of $f = 50\text{Hz}$, with the sharper peak for the 22° case again corresponding to vortex shedding.

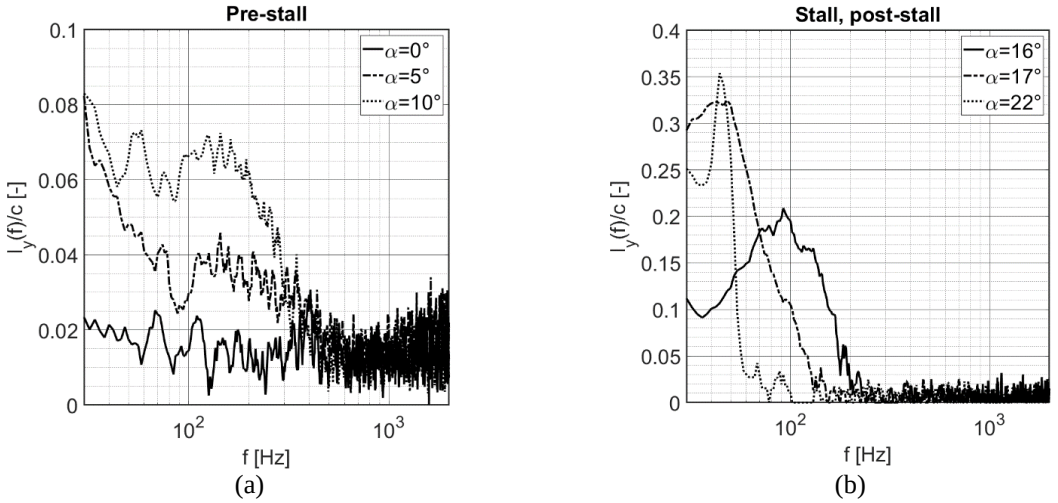

Figure 10: NACA 16-616 spanwise coherence length variation with angle of attack: (a) pre-stall, and (b) post-stall.

The spanwise coherence length variation with angle of attack of the NACA 16-506 airfoil is shown in Figure 11. Spectral shape in the pre-stall regime is consistent between each angle of attack although the peak length increases with increasing angle of attack, consistent with the length scale of the dominant turbulent structures increasing as the boundary layer grows. Post-stall, the coherence length is much larger, reflecting the much larger length scales associated with separated flow. For the post-stall angles of attack the spectra at the trailing-edge is near-totally dominated by a peak associated with vortex shedding at a frequency of $f = 60\text{Hz}$.

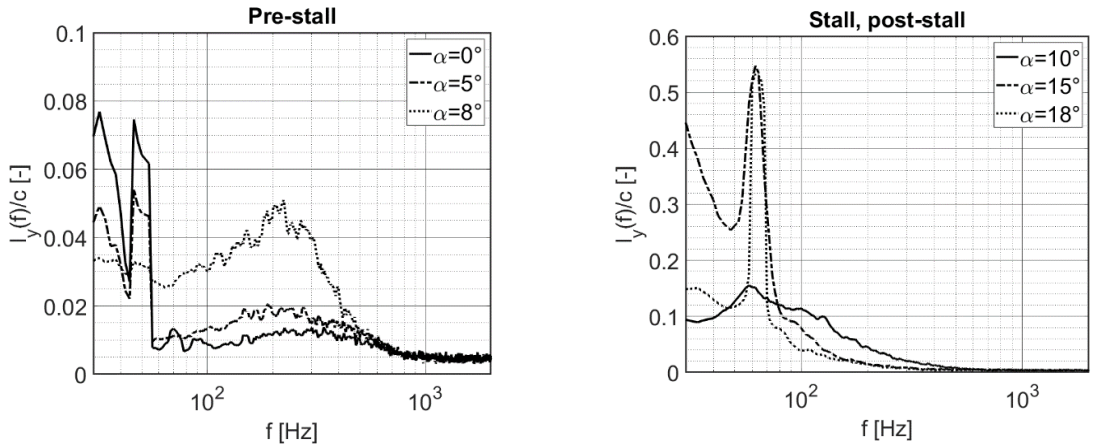

Figure 11: NACA 16-506 spanwise coherence length variation with angle of attack: (a) pre-stall, and (b) post-stall.

The NACA 0024 spanwise coherence length variation with angle of attack, shown in Figure 12, is generally similar in behavior to the other two airfoils with the coherence length post-stall being far greater in magnitude than pre-stall. One difference however is that the coherence length at 10° angle of attack is greater than for the still pre-stall 15° angle of attack. Though this is counter-intuitive it is likely due to the occurrence of localized separation for the 15° angle of attack case.

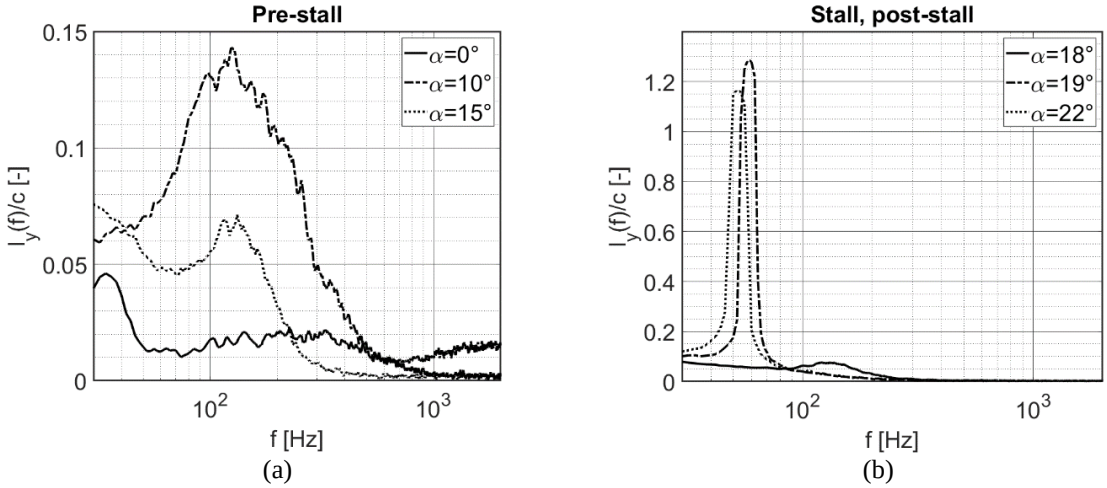

Figure 12: NACA 0024 spanwise coherence length variation with angle of attack: (a) pre-stall, and (b) post-stall.

VI. Boundary Layer Velocity Results

In this section, hot-wire anemometry results recorded for the NACA 16-616 and NACA 16-506 airfoils are examined at multiple angles of attack. The results are presented in the form of suction surface boundary layer profiles, providing a direct indication of the nature of the flow within the boundary layer and in particular, whether it is attached, mildly separated, or fully separated.

Figure 13 shows the NACA 16-616 suction surface boundary layer velocity profiles at three chordwise positions for four angles of attack: $\alpha = 0°, 10°, 16°$, and 22°. At 0° angle of attack, for the two mid-chord locations of $x/c = 0.6$ and 0.75, the boundary layers are clearly attached with a 99% boundary layer thickness of $\delta = 0.012c$ and $0.018c$, respectively. The boundary layer at the trailing-edge location of $x/c = 0.98$ however is much larger, although still attached, with a thickness of $\delta = 0.055c$. At the same three chordwise positions but at 10° angle of attack, the

boundary layers are again still clearly attached at the $x/c = 0.6$ and 0.75 locations with thicknesses of $\delta = 0.021c$ and $0.032c$, respectively. However, for the trailing-edge location of $x/c = 0.98$, the clear inflection point in the boundary layer profile indicates reversed flow and hence suggests strongly that separation has occurred, corroborating the findings in the surface pressure fluctuations sections of this report, and further reinforcing the suggestion of a trailing-edge separation mechanism. The velocity profiles at 16° angle of attack show similar behavior at the three chordwise locations to the 10° case, with attached flow at the two further upstream chordwise locations and separated flow at the trailing-edge. As expected, the attached boundary layers are larger with thicknesses of $\delta = 0.062c$ and $0.11c$ at $x/c = 0.6$ and 0.75, respectively, and the separated region at the trailing-edge has grown from $\delta = 0.098c$ for the 10° case to $\delta = 0.22c$ for the 16° case. Finally, the boundary layer profiles at 22° angle of attack show that the flow is fully separated at all three chordwise locations, reflecting the fully stalled nature of the airfoil at this angle of attack.

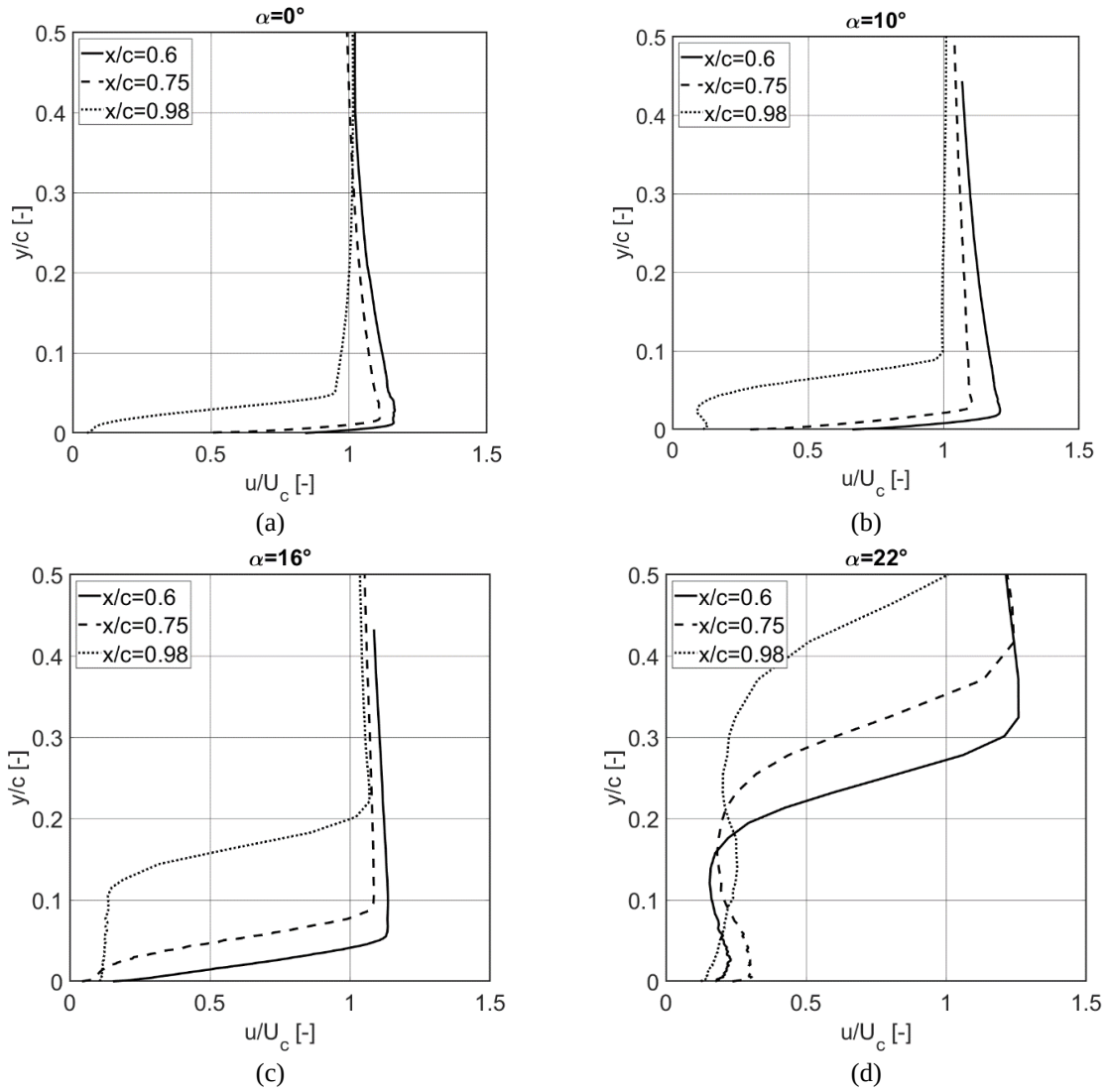

Figure 13: NACA 16-616 boundary layer velocity profiles at: (a) $\alpha = 0°$, (b) $\alpha = 10°$, (c) $\alpha = 16°$, and (d) $\alpha = 22°$ angles of attack.

Boundary layer velocity profiles for the NACA 16-506 airfoil are presented in Figure 14 below for four angles of attack at two chordwise positions on the airfoil suction surface. For the two pre-stall regime angles of attack, i.e., 0° and 8°, the velocity profiles are typical of attached boundary layers, with boundary layer growth evident towards the trailing-edge and as the angle of attack is increased. This is in contrast to the NACA 16-616 airfoil where small-scale

separation was indicated at the trailing-edge, even within the pre-stall regime. The boundary layer profiles at 10° angle of attack, i.e., at the upper limit of the stall regime, show interesting behavior as the flow is clearly separated at the further upstream location yet appears to still be attached at the trailing-edge. This is likely due to the thin-airfoil stall mechanism where a separation bubble develops over the mid-chord, including $x/c = 0.3$ but not $x/c = 0.95$ in this case, before eventually "bursting" and leading to flow separation across the airfoil chord, as is evident in the fully stalled 18° angle of attack case.

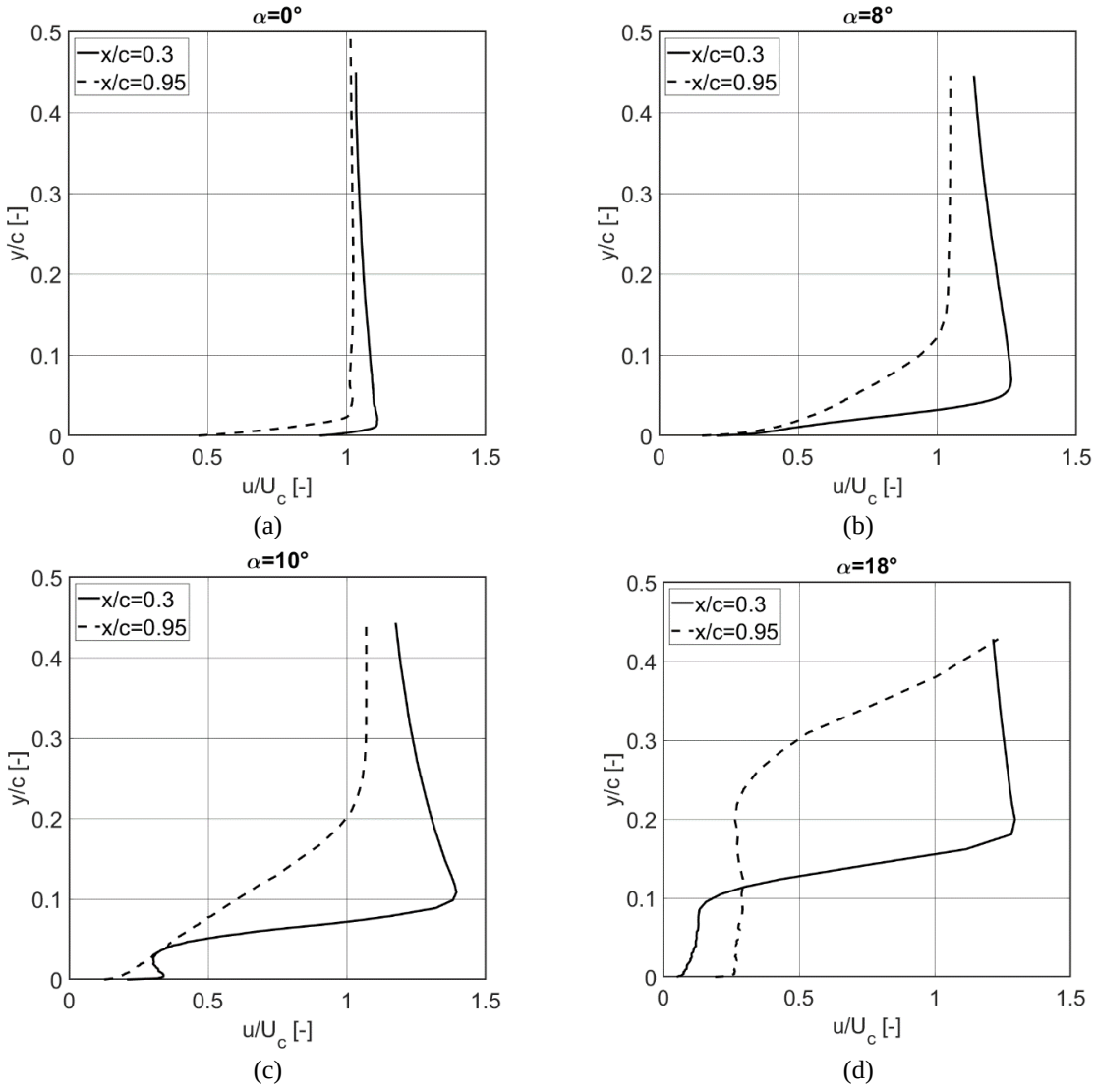

Figure 14: NACA 16-506 boundary layer velocity profiles at: (a) α=0°, (b) α=8°, (c) α=10°, and (d) α=18° angles of attack.

VII. Far-field sound from Amiet's Model

This section of the paper presents a theoretical prediction of the far-field sound radiated by the three airfoils, modelled using Amiet's method [3]. Amiet's model takes as an input a statistical description of the convecting surface pressure distribution with the key, underpinning, assumption that the turbulent velocity field is unaffected by the geometrical discontinuity at the trailing-edge, i.e. that the turbulence remains statistically stationary as it passes over the trailing-edge. In Amiet's model, the far-field noise spectrum at an observer position $\boldsymbol{x}$, $SPL(f, \boldsymbol{x})$, is given by

$$SPL(f, \boldsymbol{x}) = D(f, \boldsymbol{x})|\mathcal{L}(f)|^2 l(f)\phi_{pp}(f), \quad (1)$$

where $\phi_{pp}(f)$ is the surface pressure spectrum at the trailing-edge, $l(f)$ is the spanwise coherence length, which quantifies the spanwise extent of turbulent structures in the boundary layer, $D(f, \boldsymbol{x})$ is a radiation term, and $|\mathcal{L}(f)|$ is the acoustically weighted airfoil response function.

Figure 15 shows the prediction of the radiated far-field sound for each airfoil in the pre-stall regime and the stall and post-stall regimes. The stark impact of stall on the sound produced by each airfoil is immediately apparent, as is the impact of airfoil shape for a given flow regime. For each airfoil, predicted low frequency sound pressure levels are shown to increase as the airfoil stalls although the nature of the increase is airfoil dependent. For the NACA 16-616 and NACA 0024 airfoils, a significant increase occurs only for frequencies below $f = 200$Hz and $f = 300$Hz respectively, whereas for the NACA 16-506 airfoil the sound pressure levels are significantly increased for all frequencies below $f = 1$kHz. The similarity in behavior between the two thicker NACA 16-616 and NACA 0024 airfoils is likely due to both airfoils experiencing a small-scale separation near to the trailing-edge in the pre-stall regime, effectively lessening the abrupt impact of stall on the flow at the trailing-edge. Conversely, the NACA 16-506 airfoil experiences no such localized separation and consequently stall has a significant and abrupt effect on the flow at the trailing-edge and consequently the predicted far-field sound.

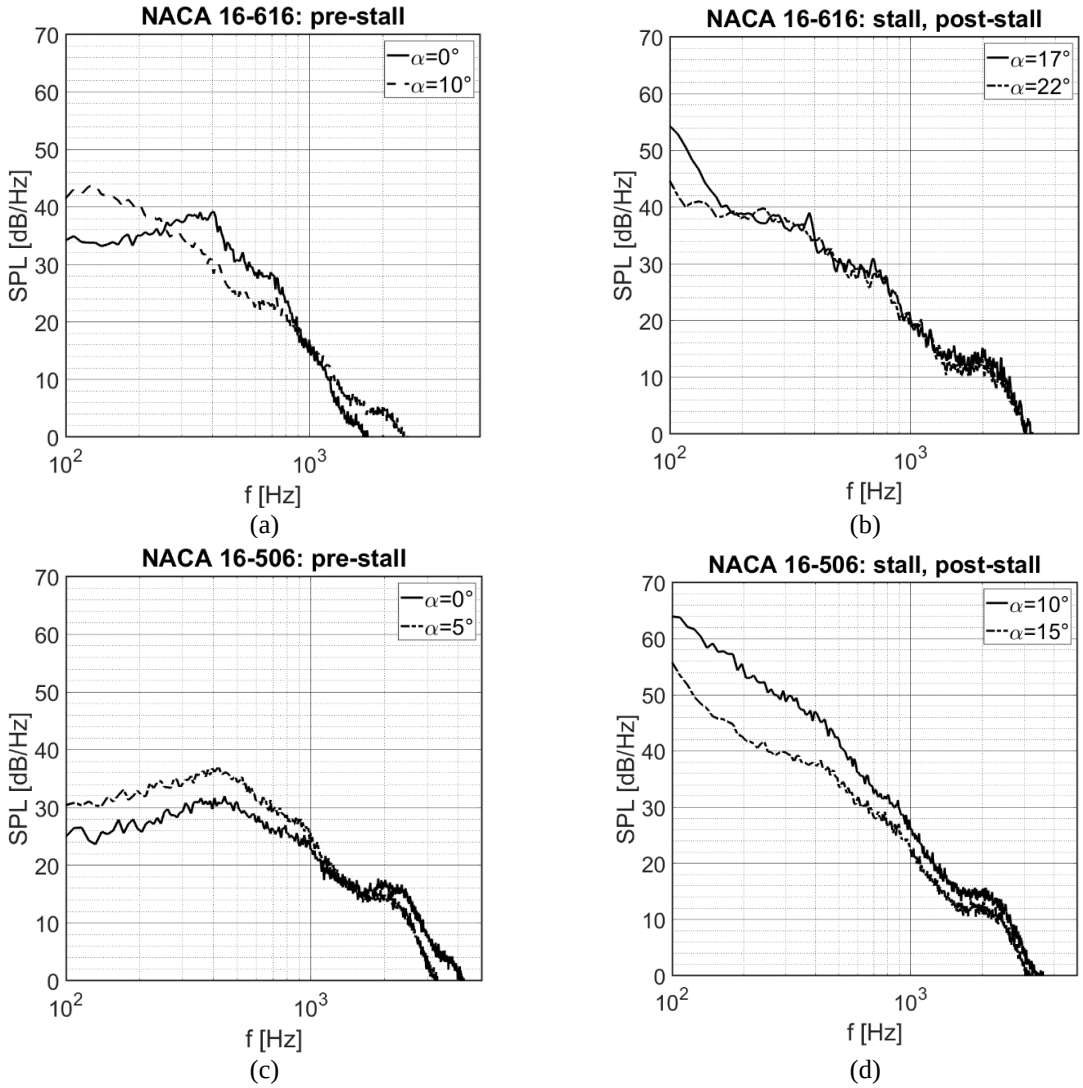

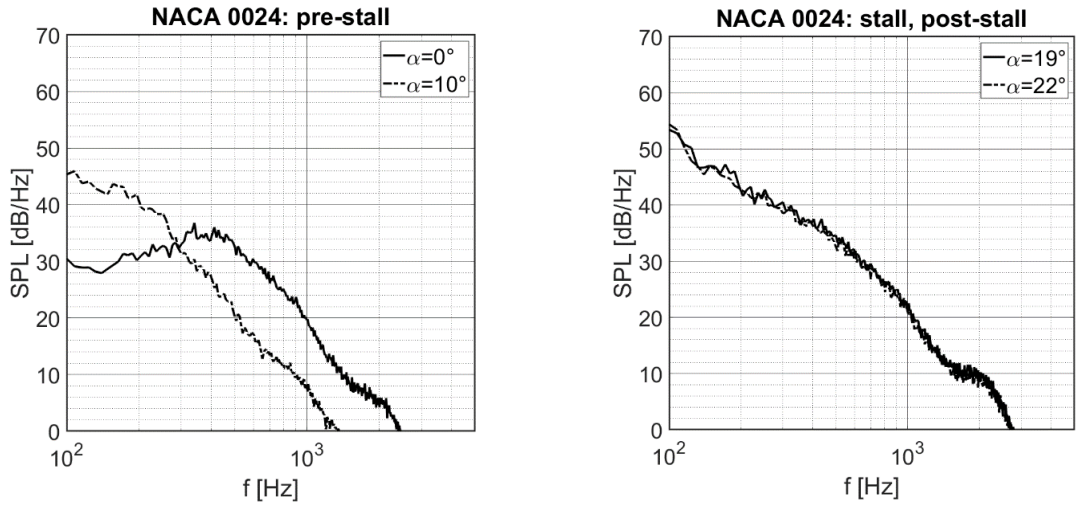

Figure 15: Prediction of radiated far-field sound pressure level based on Amiet's model for: (a) NACA 16-616 pre-stall regime, (b) NACA 16-616 stall and post-stall regimes, (c) NACA 16-506 pre-stall regime, (d) NACA 16-506 stall and post-stall regimes, (e) NACA 0024 pre-stall regime, and (f) NACA 0024 stall and post-stall regimes.

VIII. Conclusion

Airfoil stall noise is a comparatively under-researched area within the field of aeroacoustics and consequently, there is limited data of it and few models for it. The primary purpose of the present study is to generate near-field hydrodynamic data for a range of airfoils and to investigate the effect of airfoil shape and stalling behavior on the predicted radiated far-field sound. To this end, this paper has presented an investigation of the hydrodynamic near-field and predicted radiated acoustic far-field for three airfoils: NACA 16-616, NACA 16-506, and NACA 0024 profiles. For each airfoil, three distinct flow regimes have been identified in the near-field static pressure and unsteady pressure fluctuation data, and additionally the stalling behavior for each has been identified. It has been demonstrated that airfoil shape has a significant impact on the near-field behavior, particularly with regards to the stalling behavior where the thicker NACA 16-616 and NACA 0024 airfoils are found to experience a secondary trailing-edge separation mechanism in addition the dominant leading-edge separation. Using Amiet's model, the radiated acoustic far-field has been predicted for each airfoil and the effect of airfoil shape and stalling behavior on the sound has been demonstrated, with the thicker airfoils experiencing a less abrupt increase in predicted low frequency sound pressure levels likely due to the influence of the secondary trailing-edge separation mechanism. The dependency of predicted radiated far-field sound on airfoil shape underlines the importance of the use of a broad dataset when developing models of airfoil stall noise.

Acknowledgments

The authors would like to acknowledge the financial support from the Engineering and Physical Sciences Research Council (EPSRC) for the present study via research Grant No. EP/R010846/1, and the first author would also like to acknowledge the support for the PhD studentship from Dowty Propellers and Embraer.

References

[1] M. Roger and S. Moreau, "Back-scattering correction and further extensions of Amiet's trailing-edge noise model. Part 1: theory," *Journal of Sound and Vibration,* vol. 286, p. 477:506, 2005.

[2] J. E. Ffowcs Williams and L. H. Hall, "Aerodynamic sound generation by turbulent flow in the vicinity of a scattering half plane," *Journal of Fluid Mechanics,* vol. 40, pp. 657-670, 1970.

[3] R. K. Amiet, "Noise Due to Turbulent Flow Past a Trailing Edge," *Jounral of Sound and Vibration,* vol. 47, pp. 387-393, 1976.

[4] M. S. Howe, "A review of the theory of trailing edge noise," *Journal of Sound and Vibration,* vol. 61, no. 3, pp. 437-465, 1978.

[5] Y. D. Mayer, B. Lyu, H. Kamliya Jawahar and M. Azarpeyvand, "A semi-analytical noise prediction model for airfoils with serrated trailing edges," *Renewable Energy,* vol. 143, pp. 679-691, 2019.

[6] M. Roger and S. Moreau, "Back-scattering correction and further extensions of Amiet's trailing-edge noise model. Part II: Application," *Journal of Sound and Vibration,* vol. 323, no. 1-2, pp. 397-425, 2009.

[7] M. Szőke and M. Azarpeyvand, "Effect of Inclined Transverse Jets on Trailing-Edge Noise Generation," *Physics of Fluids,* vol. 30, no. 8, p. 085110, 2018.

[8] A. Laratro, M. Arjomandi, B. Cazzolato and R. Kelso, "Self-noise and directivity of simple airfoils during stall: An experimental," *Applied Acoustics,* vol. 127, pp. 133-146, 2017.

[9] Y. Mayer, B. Zang and M. Azarpeyvand, "A preliminary study of dynamic stall noise," in *AIAA Scitech 2020 Forum*, Orlando, Florida, 2020.

[10] S. Bianchi, A. Corsini, A. G. Sheard and C. Tortora, "A Critical Review of Stall Control Techniques in Industrial Fans," *ISRN Mechanical Engineering,* pp. 1-18, 2013.

[11] A. Laratro, M. Arjomandi, R. Kelso and B. Cazzolato, "A discussion of wind turbine interaction and stall contributions to wind farm noise," *Journal of Wind Engineering and Industrial Aerodynamics,* vol. 127, pp. 1-10, 2014.

[12] S. Moreau, M. Roger and J. Cristophe, "Flow Features and Self-Noise of Airfoils Near Stall or in Stall," in *AIAA Aeroacoustics Conference*, Miami, Florida, 2009.

[13] M. R. Fink and D. A. Bailey, "Airframe Noise Reduction Studies and Clean-Airframe Noise Investigation," NASA, 1980.

[14] Y. Maruta and S. Kotake, "Separated flow noise of a flat plate at large attack angles," *Journal of Sound and Vibration,* vol. 89, pp. 335-357, 1983.

[15] S. Oerlemans, "Wind turbine noise: primary noises," Nationaal Lucht- en Ruimtevaartlaboratorium, Amsterdam, The Netherlands, 2011.

[16] W. K. Blake, Mechanics of Flow-Induced Sound and Vibration, Vol.I and II, New York: Academic Press, 1986.

[17] R. R. Parchen, "Progress report DRAW: A prediction scheme for trailing edge noise based on detailed boundary layer characteristics," TNO Institute of Applied Physics, The Netherlands, 1998.

[18] F. Bertagnolio, H. A. Madsen, A. Fischer and C. Bak, "A semi-empirical airfoil stall noise model based on surface pressure measurements," *Journal of Sound and Vibration,* vol. 387, pp. 127-162, 2017.

[19] G. Lacagnina, P. Chaitanya, J.-H. Kim, T. Berk, P. Joseph, K.-S. Choi, B. Ganapathisubramani, S. M. Hasheminejad, T. P. Chong, O. Stalnov, M. F. Shahab, M. Omidyeganeh and A. Pinelli, "Leading edge serrations for the reduction of airfoil self-noise at low angle of attack, pre-stall and post-stall conditions," *International Journal of Aeroacoustics,* vol. 20, no. 1-2, pp. 130-156, 2021.

[20] T. F. Brooks, D. S. Pope and M. A. Marcolini, "Airfoil Self-Noise and Prediction," NASA Reference Publication, 1989.

[21] M. De Gennaro and H. Kuehnelt, "Broadband Noise Modelling and Prediction for Axial Fans," in *International Conference on Fan noise, Technology and Numerical Methods*, Senlis, France, 2012.

[22] S. Oerlemans and J. G. Schepers, "Prediction of wind turbine noise and validation against experiment," *Noise Notes,* vol. 9, no. 2, pp. 3-28, 2010.

[23] Y. D. Mayer, H. Kamliya Jawahar, M. Szőke, S. A. Showkat Ali and M. Azarpeyvand, "Design and performance of an aeroacoustic wind tunnel facility at the University of Bristol," *Applied Acoustics,* vol. 155, pp. 358-370, 2019.

[24] W. J. Devenport, R. A. Burdisso, A. Borgoltz, P. A. Ravetta, M. F. Barone, K. A. Brown and M. A. Morton, "The Kevlar-walled anechoic wind tunnel," *Journal of Sound and Vibration,* vol. 332, no. 17, pp. 3971-3991, 2013.

[25] S. Yarusevych, P. E. Sullivan and J. G. Kawall, "On vortex shedding from an airfoil in low-Reynolds-number flows," *Journal of Fluid Mechanics,* vol. 632, pp. 245-271, 2009.